A Computational Framework for the Statistical Analysis of Cardiac Diffusion Tensors: Application to a Small Database of Canine Hearts.

Jean-Marc Peyrat*, Maxime Sermesant, Xavier Pennec, Hervé Delingette,
Chenyang Xu, Elliot R. McVeigh and Nicholas Ayache

***Abstract*—We propose a unified computational framework to build a statistical atlas of the cardiac fiber architecture from diffusion tensor magnetic resonance images (DT-MRIs). We apply this framework to a small database of nine *ex vivo* canine hearts. An average cardiac fiber architecture and a measure of its variability are computed based on most recent advances in diffusion tensor statistics. This statistical analysis confirms the already established good stability of the fiber orientations and a higher variability of the laminar sheet orientations within a given species. The statistical comparison between the canine atlas and a standard human cardiac DT-MRI shows a better stability of the fiber orientations than their laminar sheet orientations between the two species. The proposed computational framework can be applied to larger databases of cardiac DT-MRIs from various species to better establish intra- and inter-species statistics on the anatomical structure of cardiac fibers. This information will be useful to guide the adjustment of average fiber models onto specific patients from *in vivo* anatomical imaging modalities.**

***Index Terms*—Atlas, cardiac, diffusion tensor magnetic resonance imaging, DTI, DT-MRI, fiber architecture, heart, laminar sheets, statistics.**

I. INTRODUCTION

CARDIAC fiber architecture, a complex arrangement of myofibers bounded to each other to form laminar sheets [1], plays an essential role in defining the electrical and mechanical behavior of the heart [2], [3]. Mathematical modeling of the cardiac fiber architecture and its variability is important to better understand physiological principles and to construct computational models of the heart [4], [5]. However, the *in vivo* imaging of the cardiac fiber architecture at high resolution is still considered to be infeasible in the near term because of heart motion and limitations in current imaging techniques [6], [7]. Therefore, modeling of the cardiac fiber architecture and its variability on *ex vivo* data is particularly important. For instance, the fiber architecture model can be used to simulate the electrical and mechanical functions of the heart for planning patient-specific therapies [8], [9].

Until recently, the modeling of the cardiac fiber architecture mostly came from studies of histological slices [10], [11]. They revealed the common features between species such as the transmural variation of the fiber and laminar sheet orientations parameterized by the inclination angle (also known as elevation angle) and the intersection angle [1]. However, the definition of these angles was limited by the 2D nature of histological slices, whose accurate reconstruction in 3D is not straightforward [12]. Measurements of fiber architecture have been eased by the use of diffusion tensor magnetic resonance imaging (DT-MRI) [13], [14]. Indeed, a correlation between the cardiac fiber structure and diffusion tensors has been demonstrated: the primary eigenvector of the diffusion tensor is locally aligned with the fiber direction [15], [16] as is the tertiary eigenvector with the laminar sheet normal [17]–[19]. Thus, DT-MRI provides directly a 3D description of the fiber architecture in a shorter time but at a lower resolution compared to histological studies. In the past years several authors have performed studies on the variability of fiber [20]–[22] and laminar sheet [18]–[21], [23] orientations using DT-MRI. They have been so far limited to features extracted from diffusion tensors such as scalar values (for instance, inclination and intersection angles [18], [19], [23]) or vector values (primary eigenvector [22] only describing the fiber orientation). From these studies, different models of the cardiac fiber architecture were proposed and used for electromechanical simulations: a synthetic model based on general observations of the common features in mammalian hearts [24], a model based on the 3D reconstruction of the fiber orientation of a canine heart from histological studies [11], and a single DT-MRI acquisition of an *ex vivo* canine heart [25]. These models are either too generic and simplistic or too specific to accurately describe the detailed anatomy and its inter-subject variability.

To improve these models, a framework to build very high resolution 3D models of the cardiac fiber architecture from histological studies has been proposed without experimental validation [26]. Here, we propose a unified computational framework to build an atlas of the cardiac fiber architecture

---

Manuscript received January 14, 2007; revised August 8, 2007. This work was supported by Siemens Corporate Research, Princeton, NJ, USA. *Asterisk indicates corresponding author.*

*J.-M. Peyrat is with the INRIA, Asclepios Research Project, 2004, route des Lucioles, BP 93, 06902 Sophia-Antipolis Cedex, France (email: jean-marc.peyrat@inria.fr).

M. Sermesant is with the INRIA, Asclepios Research Project, Sophia-Antipolis, France, and with King's College London, Cardiac MR Research Group, Guy's Hospital, London, UK

X. Pennec, H. Delingette and N. Ayache are with the INRIA, Asclepios Research Project, Sophia-Antipolis, France.

C. Xu is with Siemens Corporate Research, Department of Imaging and Visualization, Princeton, NJ 08540 USA.

E. R. McVeigh is with the Laboratory of Cardiac Energetics, NHLBI, National Institute of Health, DHHS, Bethesda, MD 20892 USA, and with the Department of Biomedical Engineering, Johns Hopkins University, Baltimore, MD 21205 USA.

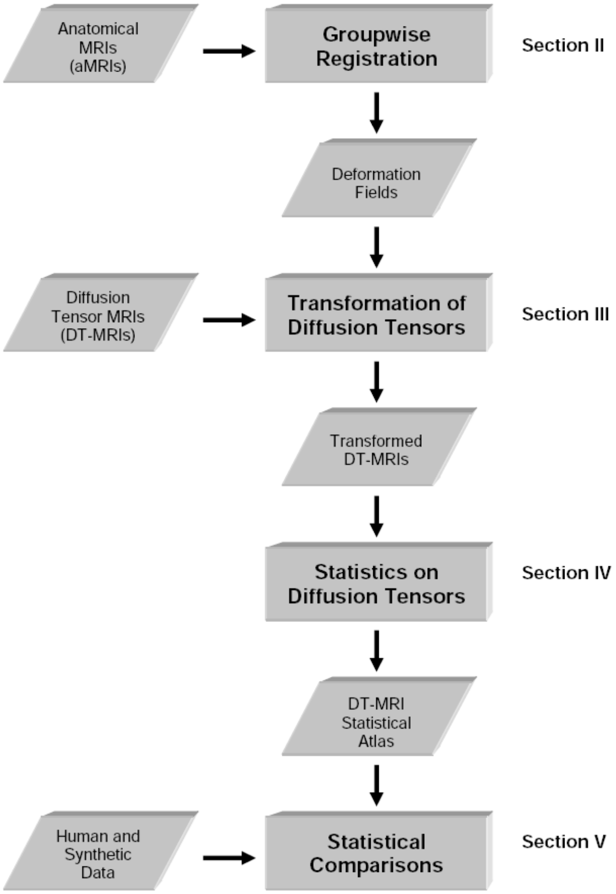

Fig. 1. Overall workflow of the proposed framework to build a DT-MRI atlas that is compared to human and synthetic data.

that is learned statistically from a population of DT-MRIs. Our approach differs from previous cardiac studies in computing statistics directly on the diffusion tensors that contains the whole fiber structure information. However, since diffusion tensors are symmetric positive definite matrices that do not lie on a vector space, classical Euclidean multivariate statistics are not consistent with the positivity constraint on the eigenvalues. Riemannian geometry, based on either affine-invariant [27]–[31] or Log-Euclidean [32] metrics, gives a general and consistent computational framework. Statistics on diffusion tensors have already been used to build brain atlases. But none of them defined a complete and consistent framework with the most recent advances on diffusion tensor processing. Jones *et al.* [33] computed first-order statistics with a Euclidean metric. Their second-order statistics were limited to features of the diffusion tensor (the dyadic tensor [34] formed from the primary eigenvector). Second-order statistics on the whole diffusion tensor were computed for model-based diffusion tensor tractography [35] in the brain but only with a Euclidean metric. A population study of brain diffusion tensors used statistics with the Log-Euclidean metric but was limited to their averaging [36].

Unlike previous works on statistical analysis of DT-MRIs, the proposed computational framework is both complete and consistent in terms of the following three aspects. First, we use a Riemannian metric to be consistent with the positivity constraint on the eigenvalues. Second, we compute the average and covariance matrix of the whole diffusion tensors. Third, we employ new tools to extract the variabilities of the eigenvectors and eigenvalues from the covariance matrix. These tools are better suited for studying the variability of cardiac fiber and laminar sheet orientations.

A first preliminary study showed the feasibility of such a statistical atlas on the ventricles with downsampled images [37]. Here, we perform an extended study by using more *ex vivo* canine hearts at the full image resolution and including whole heart. The resulting atlas[1] provides an average cardiac fiber architecture and its variability within a population. Then, we evaluate the advantages of the average cardiac fiber architecture directly built from real data over a synthetic model based on a generalization of the observations in different studies. As mentioned previously, the *in vivo* acquisition of high resolution cardiac DT-MRI is made difficult by heart motion. Furthermore, since healthy hearts are preferred to be transplanted rather than used for research purposes, *ex vivo* DT-MRI acquisition is very rare. The exceptional access to a single *ex vivo* human cardiac DT-MRI allows us to perform a preliminary inter-species comparison before a larger database is available.

We present here an overview of the workflow (see Fig. 1):

- *Groupwise registration of anatomical MRIs (Section II)*. To compare different hearts, we first need to find an inter-subject mapping for normalizing their geometries. This mapping is obtained from a groupwise registration of anatomical MRIs. To ensure the accuracy of the atlas we build, matching corresponding anatomical structures is necessary. Thus, we propose to include interactive guidance of pairwise registrations [38] in a classical worklow for atlas building [39].
- *Transformation of diffusion tensor fields (Section III)*. Once a mapping between the hearts is known, an important issue is to transform the diffusion tensors properly. These tensors contain a directional information of diffusion linked to the reference frame of the image. When transforming an image, this reference frame is modified. Thus, the diffusion tensors have to be transformed according to the modification of the reference frame. Different transformation strategies have been proposed [40]. We compare these strategies on synthetic and experimental data to characterize their impacts on diffusion tensors and give insights on how to determine the most suited transformation strategy.
- *Complete and consistent statistics on diffusion tensors (Section IV)*. This is realized by computing average diffusion tensors and their corresponding covariance matrices using the Log-Euclidean framework. The difficulty is to interpret directly the covariance matrix of diffusion tensors, especially in terms of cardiac fiber architecture. Thus, we propose new efficient tools to extract from this covariance matrix the variability of the eigenvectors and eigenvalues.

---

[1] available at http://www-sop.inria.fr/asclepios/data/heart

- *Intra- and inter-species comparisons (Section V).* We apply this framework to perform an intra-species comparison building a statistical atlas of cardiac fiber architecture from a small database of nine canine hearts. This atlas is compared to a synthetic model of the fiber orientation [8] showing that the proposed statistical model of the cardiac fiber architecture is more complete and accurate. Finally, we perform a quantitative inter-species comparison between this atlas of canine hearts and a human heart. The results confirm a better inter-species coherence of the fiber orientations than the laminar sheet orientations.

II. REGISTRATION OF ANATOMICAL MRIs

Registering the geometries based on the DT-MRIs [41]–[44] implies a minimization of the differences between diffusion tensors. In this case, we make the assumption that there are similarities between cardiac DT-MRIs. Actually, quantifying these similarities is exactly what we want to evaluate in the following statistical analysis. To avoid introducing a bias, we register the unweighted images of the DT-MRI acquisition that only hold anatomical information. Furthermore, these anatomical MRIs have the advantage to be acquired in the same geometry as the DT-MRIs without distortion. Thus, the deformation fields used to transform the anatomical MRIs can be directly used to transform the DT-MRIs.

To register the anatomical MRIs to an average geometry, we propose here a classical workflow for atlas building. First, we present a pairwise registration algorithm allowing interactive guidance that ensures the quality of the inter-subject mapping. Second, we describe an alternate groupwise registration of the anatomical MRIs relying on pairwise registration steps.

A. Pairwise Registration

The mapping of *ex vivo* hearts is challenging due to large differences in alignment and scale of the data. Thus, there is a need for a robust affine registration before using any non-rigid algorithm.

1) Constrained Affine Registration: We perform an interactive affine transformation to control its quality and to get an appropriate initialization for the non-rigid registration as follows. An affine transformation can be defined by four landmarks. The difficulty to find four repeatable landmarks to best normalize the geometry of the hearts limited us to use three landmarks. Thus, we constrained the affine transformation S based on three interactively located landmarks: the left ventricular apex (A_{LV}) and the two right ventriculo-septal junctions (corner points C_1 and C_2) in the valve plane orthogonal to the long axis of the heart (see Fig. 2).

We use these landmarks to define a composition of transformations $S = S_z \circ S_{xy} \circ R_{\theta_z} \circ T$ (see Fig. 2) that align the hearts and normalize their heights and radius:

- the translation T to match the centroids G and G' of the two pairs of corner points,
- the rotation R_{θ_z} around the direction of the long axis of the heart to match the directions given by the two pairs of corner points,
- the scaling S_{xy} to match the length of the line segments defined by the two pairs of corner points,
- the scaling S_z along the axis of the heart to match the two pairs of axial planes: the valve plane and the one containing the LV endocardial apex.

2) Interactive Non-Rigid Registration: Beg *et al.* [45] proposed a landmark and image intensity-based large deformation diffeomorphic metric mapping (LDDMM) method for non-rigid registration of cardiac geometries. We preferred to use another hybrid intensity- and landmark-based registration algorithm [38] that is well suited for fast interactive corrections. The interactive guidance by a selection of pairs of landmarks is useful to control the registration and avoid the matching of different structures. The advantage of this hybrid algorithm is to combine easily any intensity- and landmark-based registration algorithms. It relies on an iterative dual energy minimization that yields to the deformation field T, which is a weighted-average of the fitting of intensity Q_1 and landmarks Q_2:

$$T(X) = (1 - \lambda(X))[K_1 * Q_1(X)] + \lambda(X)[K_2 * Q_2(X)]$$

with X being the voxel position in the reference space, K_1 and K_2 being regularization kernels for each deformation field Q_1 and Q_2, and $\lambda(X) \in [0, 1]$ being a confidence map across the image defining the trust in the deformation fields Q_1 versus Q_2. This confidence map is a mixture of 3D normalized Gaussian centered on each landmark in the reference space and whose variance depends on its distance to the corresponding landmark. We used here a combination of thin-plate splines [46] and a diffeomorphic registration algorithm [47] based on the mutual information.

Finally, the pairwise registration is the composition of the constrained affine transformation S with the non-rigid deformation T that can be used in the groupwise registration as follows.

B. Groupwise Registration

The groupwise registration is not trivial since the average geometry and its mapping with the subject geometries are interrelated. Guimond *et al.* [39] proposed an alternate approach that was adapted by Helm *et al.* [48] to build an average cardiac geometry. All the subjects are registered to the same current reference geometry which is then updated by the new mapping to converge to an average geometry. Avants *et al.* [49] presented a recursive approach where the current reference geometry is updated each time a subject is mapped. Joshi *et al.* [50] find simultaneously an average geometry and the mapping of the subjects to it by sequentially minimizing an energy with respect to these mappings. We preferred the alternate approach to ease the introduction and the control of the guidance with pairs of landmarks. This method has the advantage to register all the subjects to the same reference geometry and thus to ensure that the interactive guidance is as meaningful as possible for the final average geometry. In the other methods, the guidance of the registration to the final average geometry would not be clear since pairs of landmarks would be set with different reference geometry for each subject.

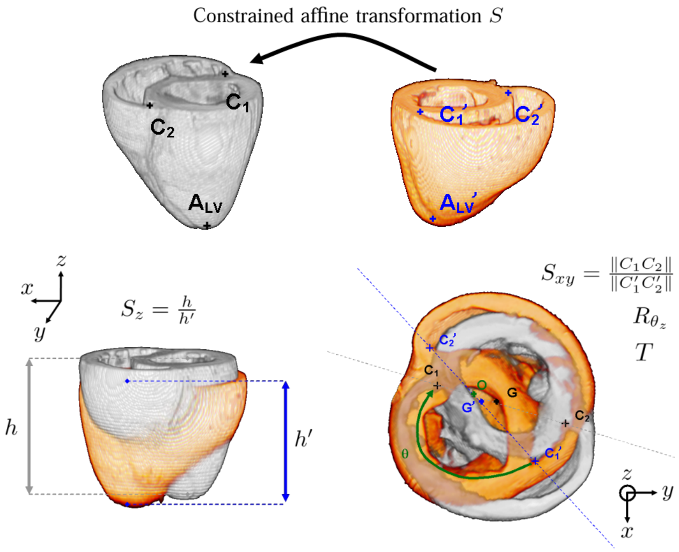

Fig. 2. The pairwise registration is initialized with a constrained affine transformation S based on the matching of three interactively located landmarks: the left ventricular apex (A_{LV}) and the two corners of the right ventricle in the valve plane (C_1 and C_2). This transformation is defined as a composition of a translation T, a rotation R_{θ_z}, a radial scaling S_{xy} and a long axis scaling S_z. The atria are not shown here for a better visualization of the landmarks.

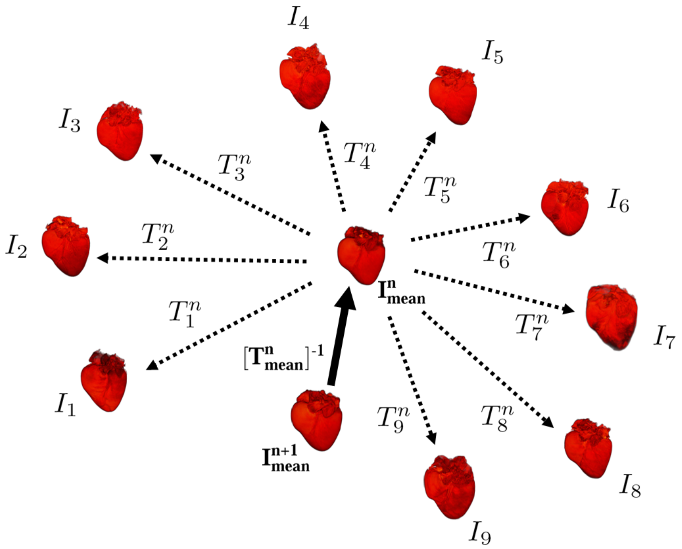

Fig. 3. The groupwise registration of the anatomical MRIs $\{I_i\}_{i=1,\ldots 9}$ is adapted from the algorithm proposed by Guimond *et al.* [39]. This algorithm is based on an alternate registration process using the resulting average geometry I^{n+1}_{mean} as a reference for the next step. The deformation fields $\{T_i^n\}_{i=1,\ldots 9}$ at the step n are a composition of a constrained affine transformation and a non-rigid deformation as described in Section II-A.

We alternately build an average geometry and register the subjects to it. We first register the dataset of images $\{I_i\}_{i=1,\ldots N}$ to the current reference image I^n_{mean} of the step n based on the pairwise registration steps described previously (the initial reference image I^0_{mean} is chosen within the dataset). The resulting deformation fields T_i^n registering the initial images I_i to the current reference image I^n_{mean} are averaged. In our case the average deformation fields have been shown to be smooth enough and to have small enough deformations to be computationally invertible. One could think about improving this step using most recent advances in statistics on diffeomorphisms [51]. A least squares approximation of the inverse of the average deformation field T^n_{mean} is applied to the current reference image I^n_{mean} which then gets closer to a barycentric geometry of the dataset (see Fig. 3). The intensities are averaged in this new average geometry. Therefore, through the deformation fields T_i^n, the original geometry and intensities of each heart are taken into account in the new average heart I^{n+1}_{mean}.

One iteration can be summarized in the equation as follows:

$$I^{n+1}_{\text{mean}}(X) = \frac{1}{N}\sum_{i=1}^{N} I_i(T_i^n \circ [T^n_{\text{mean}}]^{-1}(X))$$

where X is the voxel coordinates, I_i is the anatomical MRI of the sample i, T_i^n is the deformation field matching the current average geometry I^n_{mean} to the sample I_i at the step n, $T^n_{\text{mean}} = \frac{1}{N}\sum_{i=1}^{N} T_i^n$ is the average deformation field at the step n. These steps are repeated using the new average heart I^{n+1}_{mean} as the reference geometry until it converges. In practice, a few iterations are sufficient to get a stable geometry.

Finally, the outputs of this process are an average geometry of cardiac anatomical MRIs and a dense deformation field for each heart of the dataset. Then, these deformation fields can be used to transform the DT-MRIs.

III. TRANSFORMATION OF THE DT-MRIS

Since we use the unweighted image of the DT-MRI acquisition as the anatomical MRI, the DT-MRIs and the anatomical MRIs are in the same geometry without distortion. Thus, we can directly apply to the DT-MRIs the deformation fields computed in the previous section. The transformation of DT-MRIs is more complex than anatomical MRIs. A diffusion tensor is a covariance matrix (symmetric definite positive matrix) modeling the directional distribution of diffusion rates of water molecules. This directional information is linked to the local reference frame that is modified during the transformation. To describe this distribution in the new local reference frame, a transformation of the diffusion tensor is necessary. Each of the eigenvalues describes a diffusion process in a specific direction of the fiber structure given by its corresponding eigenvector (see first column in Fig. 4). We assume that the basic structure of fibers, organized in laminar sheets, is locally preserved. It means that the transformed eigenvectors are still an orthonormal basis in the new local reference frame. This assumption is important to preserve the correlation between the transformed diffusion tensor and the underlying fiber structure. Moreover, the diffusion process in each specific directions of the fiber structure only depends on material properties of the underlying microstructure. At our scale of observation, we can consider that these material properties are intensive properties. Thus, the eigenvalues are preserved when warping the space. Finally, the transformation of the diffusion tensors can be simply described by a rotation of the eigenvectors. Different methods have been proposed to reorient diffusion tensors in the literature. We propose here to compare the reorientation strategies to understand their fundamental differences and to justify their use given the registration context.

First, we describe the most common and meaningful reorientation strategies: the *Finite Strain* (FS) and the *Preservation of the Principal Direction* (PPD) proposed by Alexander *et al.* [40]. They are defined in the case of affine transformations and extended to non-rigid deformations [40] by approximating at each voxel the deformation field T (matching the reference image to the transformed image) with an affine transformation $A = \mathrm{Id}+\nabla T$ where Id is the identity matrix and ∇ the gradient operator. Second, we point out their fundamental differences on a typical case of synthetic diffusion tensor field transformed by basic affine transformations. Third, we compare them on real cases of cardiac diffusion tensors non-rigidly transformed for experimental validation.

A. *Finite Strain (FS)*

In the FS reorientation strategy, the rotation component of the local affine transformation is used to reorient the diffusion tensors. The polar decomposition of an affine transformation A can be written as follows: $A = RU$ where R is the rotation component and U a deformation component. Actually, the rotation component is the least squares approximation of the affine transformation by a rotation and has a closed-form solution [52]: $R = (AA^t)^{-\frac{1}{2}}A$. In the case of the FS, the action of an affine transformation on a diffusion tensor D (whose operator is $\star$) is defined as follows:

$$A \star D = R_{\mathrm{FS}}(A) \cdot D \cdot {R_{\mathrm{FS}}}^t(A)$$

where $R_{\mathrm{FS}}(A)$ is the rotation component of the affine transformation A.

Since the transformation of a diffusion tensor only depends on the affine transformation A, we can infer interesting properties. For instance, we propose to compare the action of the transformation on the diffusion tensor field (whose operator is $\star$) and the action of the transformation on the gradient of diffusion tensors (whose operator is $\bullet$) in the case of a global affine transformation.

Let us consider X the voxel coordinates in the original space and D the original diffusion tensor field. Respectively $X' = AX$ and D' are their transformed values. We use here the minimal representation $\mathrm{vec}(D)$ of a diffusion tensor $D = (D_{ij})_{i,j=1,2,3}$ to take into account the multiplicity of its off-diagonal elements [29]: $\mathrm{vec}(D) = (D_{11}, \sqrt{2}D_{12}, D_{22}, \sqrt{2}D_{31}, \sqrt{2}D_{32}, D_{33})^t$. Thus, the classical Euclidean norm of this vector representation is equal to the classical Euclidean norm of the diffusion tensor.

In the space of the transformed image, we have:

$$\nabla_{X'}\mathrm{vec}(D'_{FS}(X')) = \nabla_{X'}\mathrm{vec}(A \star D(A^{-1}X'))$$

$$\nabla_{X'}\mathrm{vec}(D'_{FS}(X')) = \nabla_{X'}\mathrm{vec}(R_{\mathrm{FS}}(A) \cdot D(A^{-1}X') \cdot {R_{\mathrm{FS}}}^t(A))$$

As R_{FS} only depends on A which is constant over the space:

$$\nabla_{X'}\mathrm{vec}(D'_{FS}(X')) = A^{-1} \bullet \nabla_X \mathrm{vec}(R_{\mathrm{FS}}(A) \cdot D(X) \cdot {R_{\mathrm{FS}}}^t(A))$$

Thus:

$$A \bullet \nabla_{X'}\mathrm{vec}(D'_{FS}(X')) = \nabla_X \mathrm{vec}(A \star D(X))$$

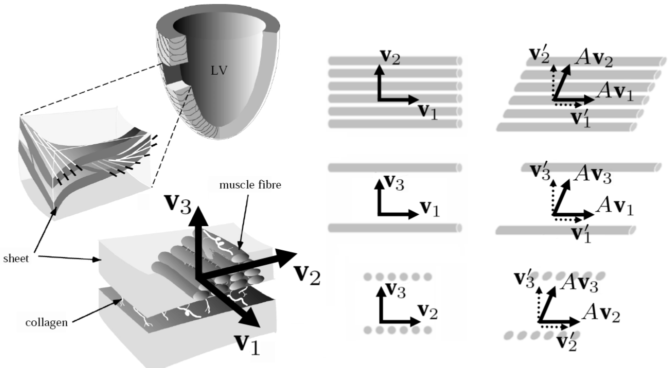

Fig. 4. [First Column] Cardiac fiber structure (adapted from LeGrice *et al.* [1]). [Second Column] Original basic fiber structure with eigenvectors $\mathbf{v}_i$. [Third Column] Example of shearing applied to the basic fiber structure: continuous arrows $A\mathbf{v}_i$ are the transformed eigenvectors through the shearing and dashed arrows $\mathbf{v}'_i$ are the eigenvectors related to the correlation between the fiber microstructure and the diffusion tensor.

The gradient of a transformed diffusion tensor field is equal to the transformed gradient of the original diffusion tensor field. Since the action of the transformation is consistent with the gradient on diffusion tensors, we expect to preserve the geometric features. We can characterize the FS reorientation strategy as a geometric transformation of the diffusion tensor fields.

B. *Preservation of the Principal Direction (PPD)*

The basic idea of the PPD reorientation strategy is to come back to the underlying microstructure described by the diffusion tensor. In the case of cardiac diffusion tensors, it has been shown [15]–[19] that the eigenvectors are linked to the fiber and laminar sheet orientations. The primary eigenvector $\mathbf{v}_1$ is aligned with the fiber direction as is the tertiary eigenvector $\mathbf{v}_3$ with the normal direction to the laminar sheet (see first column in Fig. 4). Once we have a model of the underlying microstructure, we transform it through the local affine transformation. Then, from this transformed microstructure we build the transformed diffusion tensor according to the relationship between the eigenvectors and the underlying microstructure [40].

An affine transformation can be described by a composition of basic transformations: translation, rotation, scaling and shearing. Translations and uniform scalings do not modify the orientation of the fiber structure, and the transformation of the fiber structure through rotations is obvious. Non-uniform scaling and shearing are the most problematic basic transformations to apply to the fiber structure since the amount of deformation depends on the original structure. An illustration of this dependency is shown in Fig. 4 with the action of pure shearing on the basic microstructure of cardiac fibers. The direct transformation of the original eigenvectors $\mathbf{v}_i$ leads to the vectors $A\mathbf{v}_i$ and the final transformation deduced from the deformation of the fiber structure leads to the vector $\mathbf{v}'_i$.

The fiber and laminar sheet structures are preserved when mechanically deformed by an affine transformation. Fibers are locally considered as lines and the affine transformation

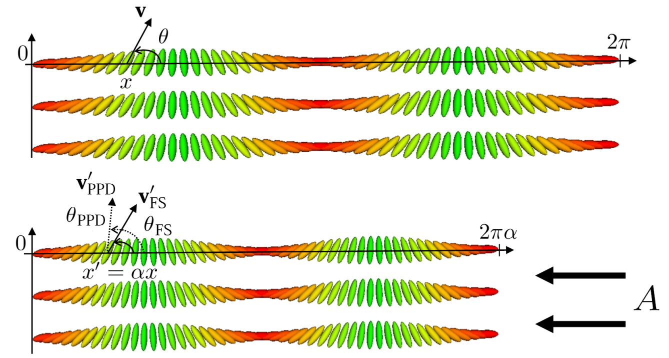

Fig. 5. Synthetic diffusion tensor field with a sinusoidal variation of the orientation θ of the primary eigenvector $\mathbf{v}$ along the direction of the x coordinates. The diffusion tensors are colored in red when the primary eigenvector is oriented along the direction of the x coordinates and in green along the direction of the y coordinates. As an illustration of the differences between the action of the FS and PPD reorientation strategies, a basic non-uniform scaling A (in this figure a compression $\alpha < 1$ along the x coordinates) is applied to the diffusion tensor field.

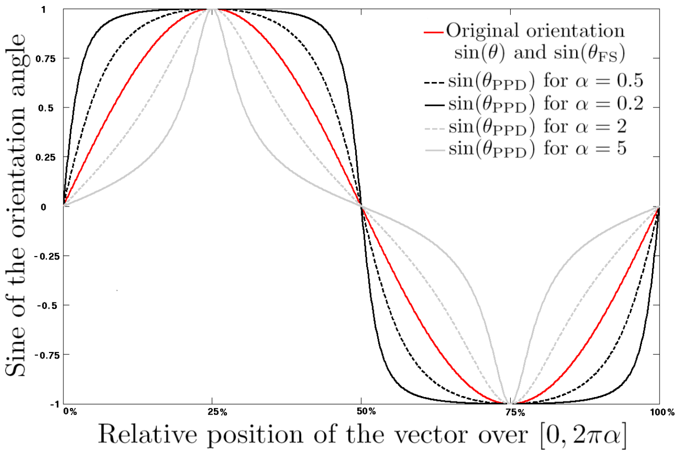

Fig. 6. Illustration of the difference between the action of the FS and PPD reorientation strategies: sine of the orientation angles θ_{PPD} and θ_{FS} of the vector field after a non-uniform scaling transformation. The orientation angle θ is the angle between the primary eigenvector and the direction of the x coordinates as described in Fig. 5. The original orientation is described by the red curve.

of a line remains a line. Thus, the new primary eigenvector $\mathbf{v}'_1$ pointing in the direction of the deformed fibers is the normalized direct transformation of the primary eigenvector $\mathbf{v}_1$ pointing in the direction of the original fibers: $\mathbf{v}'_1 = \frac{A\mathbf{v}_1}{||A\mathbf{v}_1||}$. In the same way, laminar sheets are locally considered as planes and the image of a plane through an affine transformation remains a plane. Thus, the laminar sheet is spanned by $\mathbf{v}_1$ and $\mathbf{v}_2$ and its image by $A\mathbf{v}_1$ and $A\mathbf{v}_2$. The secondary eigenvector $\mathbf{v}'_2$ lies in the laminar sheet plane and is orthogonal to the fiber direction by definition: $\mathbf{v}'_2 = \frac{A\mathbf{v}_2 - (A\mathbf{v}_2 \cdot \mathbf{v}'_1)\mathbf{v}'_1}{||A\mathbf{v}_2 - (A\mathbf{v}_2 \cdot \mathbf{v}'_1)\mathbf{v}'_1||}$. The tertiary eigenvector $\mathbf{v}_3$ is aligned locally with the normal vector of the laminar sheet plane. The normal vector of the image of a plane through an affine transformation is given by the following expression (more details in the Appendix): $\mathbf{v}'_3 = \frac{(A^{-1})^t\mathbf{v}_3}{||(A^{-1})^t\mathbf{v}_3||}$. One can easily show that this expression leads to the same result as the one proposed in [40] where they build $\mathbf{v}'_3$ from $\mathbf{v}'_1$ and $\mathbf{v}'_2$ to obtain an orthonormal frame: $\mathbf{v}'_3 = \mathbf{v}'_1 \times \mathbf{v}'_2$. This new formulation has the advantage to be independent of the computation of the other eigenvectors and to show the contravariant action of the affine transformation on the tertiary eigenvector.

The three transformed eigenvectors form an orthonormal frame. Thus, the diffusion tensor is reoriented as follows:

$$A \star D = R_{\text{PPD}}(A, D) \cdot D \cdot {R_{\text{PPD}}}^t(A, D)$$

where $R_{\text{PPD}}(A, D) = V'^t \cdot V$ is the rotation mapping the original eigenvectors $\{\mathbf{v}_i\}_{i=1,2,3}$ on the transformed eigenvectors $\{\mathbf{v}'_i\}_{i=1,2,3}$ respectively described by the matrices $V = [\mathbf{v}_1, \mathbf{v}_2, \mathbf{v}_3]$ and $V' = [\mathbf{v}'_1, \mathbf{v}'_2, \mathbf{v}'_3]$.

In this way, the PPD is by definition a mechanical transformation of the heart and its fiber architecture that for instance occurs when the heart is deformed during the cardiac cycle.

C. Comparison of the Reorientation Strategies

1) Affine Transformation of Synthetic Data: To better understand the effect of the presented reorientation strategies, we first illustrate the differences between the FS and the PPD on a simple synthetic diffusion tensor field transformed by a non-uniform scaling (see Fig. 5). To simplify the calculations and to clarify the example, we only consider the primary eigenvector of the diffusion tensors in 2D. One can easily extend this study in 3D on all the eigenvectors. Let us consider the following profile of the primary eigenvector orientations that only depends on the position along the direction of x coordinates:

$$\mathbf{v}(x) = \begin{pmatrix} \cos(x) \\ \sin(x) \end{pmatrix}$$

where $x \in [0, 2\pi]$.

We apply the following non-uniform scaling to the vector field:

$$A = \begin{pmatrix} \alpha & 0 \\ 0 & 1 \end{pmatrix}$$

Let $\mathbf{v}'_{\text{FS}}(x') = R_{\text{FS}}(A)\mathbf{v}(x)$ be the transformed vector by the FS and let $\mathbf{v}'_{\text{PPD}}(x') = R_{\text{PPD}}(A, \mathbf{v})\mathbf{v}(x)$ be the transformed vector by the PPD:

$$\mathbf{v}'_{\text{FS}}(x') = \mathbf{v}(\tfrac{x'}{\alpha})$$

$$\mathbf{v}'_{\text{PPD}}(x') = \frac{A\mathbf{v}(\frac{x'}{\alpha})}{||A\mathbf{v}(\frac{x'}{\alpha})||} = \begin{pmatrix} \frac{\alpha\cos(\frac{x'}{\alpha})}{\sqrt{\alpha^2\cos^2(\frac{x'}{\alpha}) + \sin^2(\frac{x'}{\alpha})}} \\ \frac{\sin(\frac{x'}{\alpha})}{\sqrt{\alpha^2\cos^2(\frac{x'}{\alpha}) + \sin^2(\frac{x'}{\alpha})}} \end{pmatrix}$$

where $x' \in [0, 2\pi\alpha]$.

Since the polar decomposition of a non-uniform scaling does not contain any rotation component, the orientation of the vectors is not modified using the FS reorientation strategy: $R_{\text{FS}} = \text{Id}$. Thus, only a resampling of the diffusion tensor field is performed.

We observe in Fig. 6 that the profile of vector orientation along the direction of the x coordinates is modified in the case of the PPD strategy whereas this profile is only resampled in the case of the FS strategy. The difference between these two strategies is enhanced with the importance of the compression ($\alpha < 1$) and stretching ($\alpha > 1$). This example illustrates the mechanical effect with the PPD and the preservation of geometric features with the FS. The choice of the reorientation strategy will depend on the context of the diffusion tensor transformation. If we consider that there is a mechanical transformation due to the registration process (for instance, the registration of the same heart at a different time of its cycle), we would prefer the PPD. On the other hand, if we want to preserve geometric features of the diffusion tensor field (for instance, in the case of a resampling of the heart), we would prefer the FS. The strategy used to transform the diffusion tensors will influence the statistics as follows and thus their interpretation.

We know that the transmural variation of the fiber orientation is a common feature between hearts. In our case of inter-subject comparison, we would prefer the FS to preserve this feature.

2) Non-Rigid Transformation of Real Cardiac Data: Setting up a thorough experiment to validate the choice of a reorientation strategy in the case of non-rigid transformations is not trivial. We propose here a basic experiment that could help to find practical arguments to guide the choice of the reorientation strategy. First, we register the whole cardiac dataset to a given heart. This reference heart is not transformed to minimize the influence of the reorientation strategy in the following comparisons. After registering a heart to the geometry of the reference heart, we compare the eigenvectors of the transformed DT-MRI with those of the reference image. Since both of the reorientation strategies preserve the eigenvalues, the difference between them only relies on the orientation of the transformed eigenvectors. To evaluate the accuracy of the registration to the reference DT-MRI, we compute the angular differences between the eigenvectors of the reference diffusion tensor and the transformed ones obtained from both of the reorientation strategies. This experiment is limited in the sense that only a strong difference between them would help to conclude. Indeed, these differences can be blurred by the inter-subject variability. Gathering the comparisons of 16 registrations using 2 reference hearts, 7.2% of all the registered voxels are better registered with the FS than with the PPD. Furthermore, the average angular difference of the eigenvectors is 0.3 degrees over all the voxels. These results show that the quality of the registration on experimental data is similar in both cases. Thus, we will rely on theoretical arguments to give preference to a reorientation strategy.

D. Choice of the Reorientation Strategy

Finally, we propose to rely on the three following theoretical arguments to decide which reorientation strategy is better suited for our inter-subject statistical study. First, the FS preserves the geometric features of the diffusion tensor fields. Thus, using the FS, we can directly compare these features, especially the transmural variation of the fiber orientation which is known to be a common feature between hearts. Second, the FS does not depend on the extraction of the eigenvectors whereas the PPD relies on a strong correlation between the eigenvectors and the underlying fiber structure. An error in the extraction of this structure (for instance, due to noise in the DT-MRI acquisition) could be propagated to the transformation of diffusion tensors and thus to the computed statistics. The interpretation of these statistics should take into account these errors on the transformation of diffusion tensors. Third, the FS is consistent with the Log-Euclidean metric used to compute statistics that do not depend on the reference geometry. Indeed, if the reference geometry is modified, all registered diffusion tensors in a voxel of this reference geometry are transformed with respect to the same rotation. Since the Log-Euclidean metric is rotation invariant, the statistics computed in two different reference geometries are equivalent. On the contrary, since the PPD reorientation depends on the original diffusion tensor, each of the registered diffusion tensors in a given voxel are transformed with respect to a different rotation. Thus, one can easily show that statistics computed with the Log-Euclidean metric would not be equivalent in two different reference geometries. Further studies on the comparison between the Log-Euclidean metric and a metric more consistent with the PPD transformation would be necessary. Consequently, we think that one should prefer the FS reorientation strategy in the context of inter-subject cardiac DT-MRI registration for statistical analysis to preserve geometric features, whereas the PPD reorientation strategy is better suited to the mechanical deformation during the cardiac cycle.

IV. DIFFUSION TENSOR STATISTICS

Once the DT-MRIs are transformed into the same coordinate frame, we compute their first- and second-order statistics to extract relevant information about the average diffusion tensors and their variability within a given population. Since the diffusion tensor space does not form a vector space, we cannot compute their Euclidean mean and covariance and we have chosen to use the Log-Euclidean framework to compute those statistics. Similarly, the geometric and physical interpretation of the 6×6 covariance matrix is not straightforward and we propose simple expressions to extract the variabilities of the eigenvectors and eigenvalues by projecting the covariance matrices onto proper directions. The proposed method extends previous work [34] that computes statistics on eigenvectors after extracting them from each diffusion tensor.

A. Log-Euclidean Mean and Covariance

There exists several methods to compute statistics on the diffusion tensor information. A statistical framework based on a dyadic tensor representation of eigenvalue-eigenvector pairs has been presented in [34] to reduce the bias in the estimation of the mean and variance of the eigenvalues and eigenvectors. This framework has been extended for building brain DT-MRI atlas in [33] by computing the mean, median and mode of diffusion tensors. These values are computed based on a

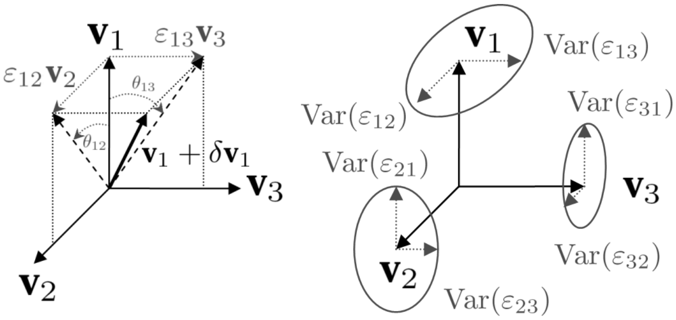

Fig. 7. [*First Column*] Increment $\delta\mathbf{v}_1$ of the primary eigenvector about its average $\mathbf{v}_1$. [*Second Column*] Orientation variability of the eigenvectors described by an ellipsoidal cone of uncertainty.

Euclidean metric that is not consistent with the nature of the diffusion tensor space. Different authors use the same affine-invariant metric based on Riemannian geometry to compute statistics on diffusion tensors for different applications: analysis of principal modes of sets of diffusion tensors [31], new anisotropic DTI index [27], [28], segmentation of diffusion tensor images [30] and the basis of a general and consistent set of algorithms for diffusion tensor processing [29]. Recently, the Log-Euclidean metric [32] has been proposed to provide a simpler and faster framework to compute consistent statistics on diffusion tensors. Indeed, the Log-Euclidean metric leads to a closed form solution whereas the computation of the affine-invariant metric is based on a minimization process.

Owing to its simplicity and low computational time, we use the Log-Euclidean metric. We compute the mean $\overline{D}_{\text{log}}$ of the transformed diffusion tensors D_i and its corresponding unbiased covariance matrix Σ [29] in the Log-space within each voxel X of the average geometry:

$$\overline{D}_{\text{log}}(X) = \exp\Big(\frac{1}{N}\sum_{i=1}^{N}\log(D_i(X))\Big)$$

$$\Sigma(X) = \frac{1}{N-1}\sum_{i=1}^{N}\mathrm{vec}(\Delta D_i(X))\cdot\mathrm{vec}(\Delta D_i(X))^t$$

where $\mathrm{vec}(\Delta D_i)$ is the minimal representation [29] of $\Delta D_i = \log(D_i) - \log(\overline{D}_{\text{log}})$ and where N is the size of the dataset. The minimal representation of a diffusion tensor $D = (D_{ij})_{i,j=1,2,3}$ is $\mathrm{vec}(D) = (D_{11}, \sqrt{2}D_{12}, D_{22}, \sqrt{2}D_{31}, \sqrt{2}D_{32}, D_{33})^t$. Thus, the classical Euclidean norm of this vector representation is equal to the classical Euclidean norm of the diffusion tensor.

B. A New Analysis of the Diffusion Tensor Covariance Matrix

The norm of the covariance matrix $\sqrt{Tr(\Sigma)}$ is actually the square root of the unbiased mean square distance of the samples to the mean diffusion tensor $\frac{1}{N-1}\sum_{i=1}^{N}\|\Delta D_i\|^2 = \frac{1}{N-1}\sum_{i=1}^{N}\mathrm{vec}(\Delta D_i)^t\cdot\mathrm{vec}(\Delta D_i)$. Since the covariance matrix is formulated in the Log-space, its norm is homogeneous to a ratio quantifying the relative variability of the whole diffusion tensor.

We are interested in gaining further insight of the variability of the whole diffusion tensor with the variability of meaningful features such as the eigenvalues and eigenvectors. We propose here new efficient tools to extract the variability of the eigenvalues and eigenvectors around their mean from the covariance matrix of diffusion tensors. The basic idea is to project the covariance matrix onto the directions given by an appropriate orthonormal basis $\{W_i\}_{i=1,\ldots 6}$ of the tangent space of the diffusion tensors manifold at the mean diffusion tensor (see Appendix for more details):

$$\begin{aligned}
W_1 &= \mathbf{v}_1\cdot{\mathbf{v}_1}^t & W_4 &= \frac{1}{\sqrt{2}}(\mathbf{v}_3\cdot{\mathbf{v}_2}^t + \mathbf{v}_2\cdot{\mathbf{v}_3}^t)\\
W_2 &= \mathbf{v}_2\cdot{\mathbf{v}_2}^t & W_5 &= \frac{1}{\sqrt{2}}(\mathbf{v}_3\cdot{\mathbf{v}_1}^t + \mathbf{v}_1\cdot{\mathbf{v}_3}^t)\\
W_3 &= \mathbf{v}_3\cdot{\mathbf{v}_3}^t & W_6 &= \frac{1}{\sqrt{2}}(\mathbf{v}_2\cdot{\mathbf{v}_1}^t + \mathbf{v}_1\cdot{\mathbf{v}_2}^t)
\end{aligned}$$

where the $\{\mathbf{v}_i\}_{(i=1,2,3)}$ are the eigenvectors of the mean diffusion tensor.

1) Eigenvalues Variability: Let us consider $\{\delta\lambda_i\}_{i=1,2,3}$ the deviation of the eigenvalues $\lambda_i = \log(d_i)$ about their mean in the Log-space. Their variances $E(\delta{\lambda_i}^2)$ can be directly formulated as the projection of the covariance matrix onto the directions of the $\{W_i\}_{i=1,2,3}$:

$$E(\delta{\lambda_i}^2) = \mathrm{vec}(W_i)^t\cdot\Sigma\cdot\mathrm{vec}(W_i)$$

These variances give directly the relative variability of the eigenvalues $\{d_i\}_{i=1,2,3}$ in the Euclidean space. We can easily study their absolute variance in the Euclidean space since $\delta d_i = d_i.\delta\lambda_i$ at the first order:

$$E(\delta{d_i}^2) = {d_i}^2[E(\delta{\lambda_i}^2)] = {d_i}^2[\mathrm{vec}(W_i)^t\cdot\Sigma\cdot\mathrm{vec}(W_i)]$$

The variances of the diffusion tensor eigenvalues in the Log-space $E(\delta{\lambda_i}^2)$ are also interesting to study since they can be linked to the normalized scatter measure of the diffusion tensors about their mean [33]. Indeed, the normalized scatter measure $\overline{S}_2$ describes a global dispersion of all the eigenvalues at the same time:

$$\overline{S}_2{}^2 = \frac{\frac{1}{N-1}\sum_{i=1}^{N}\|D_i-\overline{D}\|^2}{\|\overline{D}\|^2} = \frac{E(\|\delta D\|^2)}{\|\overline{D}\|^2} = \frac{\sum_{i=1}^{3}E(\delta{d_i}^2)}{\sum_{i=1}^{3}\overline{d}_i{}^2}$$

By contrast, the variance of the eigenvalues in the Log-space extracted from the covariance matrix gives information on the normalized dispersion of each eigenvalues about its Log-Euclidean mean independently:

$$E(\delta{\lambda_i}^2) = \frac{E(\delta{d_i}^2)}{\overline{d}_i{}^2}$$

2) Eigenvectors Variability: Let us consider $\{\varepsilon_{ij}\}_{i,j=1,2,3}$ the coordinates of the deviation $\{\delta\mathbf{v}_i\}_{i=1,2,3}$ of the eigenvectors $\{\mathbf{v}_i\}_{i=1,2,3}$ in the frame of the mean eigenvectors (see Fig. 7). These coordinates correspond to the tangent of the angle $\{\tan(\theta_{i,j})\}_{i,j=1,2,3}$ with the mean eigenvector. The projections onto the $\{W_i\}_{(i=4,5,6)}$ represent the rotation variability of the coupled orthonormal vectors $(\mathbf{v}_2,\mathbf{v}_3)$, $(\mathbf{v}_1,\mathbf{v}_3)$ and $(\mathbf{v}_2,\mathbf{v}_1)$ respectively around $\mathbf{v}_1$, $\mathbf{v}_2$ and $\mathbf{v}_3$ (see Fig. 7):

$$E(\varepsilon_{23}{}^2) = \frac{1}{2(\lambda_2 - \lambda_3)^2}[\mathrm{vec}(W_4)^t \cdot \Sigma \cdot \mathrm{vec}(W_4)]$$
$$E(\varepsilon_{13}{}^2) = \frac{1}{2(\lambda_1 - \lambda_3)^2}[\mathrm{vec}(W_5)^t \cdot \Sigma \cdot \mathrm{vec}(W_5)]$$
$$E(\varepsilon_{12}{}^2) = \frac{1}{2(\lambda_1 - \lambda_2)^2}[\mathrm{vec}(W_6)^t \cdot \Sigma \cdot \mathrm{vec}(W_6)]$$

The advantage of this formulation compared to previous works [33], [34], where they study independently the dyadic tensor corresponding to each eigenvector, is to get the eigenvectors variability knowing that they are coupled to make an orthonormal frame. We notice that these orientation variances are dependent on the distance between the eigenvalues. When two eigenvalues are close to each other, the associated eigenvectors are not well defined. Thus, high variances on eigenvectors may correspond to two different situations: either a high variability of well defined eigenvectors, or a situation where eigenvectors are not well defined. On the contrary, low variances have a unique interpretation: the eigenvectors are well defined and their variability is low. This dependence on the definition of the eigenvectors is not specific to our methodology since the one developed by [34] needs also to extract the eigenvectors to build their corresponding dyadic tensors. The main difference between the two approaches lies in the order of the computation of statistics. The dyadic tensor approach first extracts the eigenvectors before computing their statistics whereas in our method the tensor statistics are first computed before extracting the eigenvectors. Thus, in our framework, we can compute statistics on the diffusion tensor even in an isotropic case.

From those three variances $E(\varepsilon_{ij}{}^2)$, we can describe the variability of each eigenvector with an ellipsoidal cone of uncertainty (see Fig. 7) around that eigenvector. This is in contrast to the dyadic coherence κ proposed by [34] and used in brain population analysis [33] to assess the orientation dispersion around an average eigenvector $\bar{\mathbf{v}}_i$:

$$\kappa = 1 - \sqrt{\frac{\beta_2 + \beta_3}{2\beta_1}}$$

where the $\{\beta_j\}_{(j=1,2,3)}$ are the eigenvalues of the mean dyadic tensors $\overline{\mathbf{v}_i \cdot \mathbf{v}_i^t}$ of the diffusion eigenvectors $\mathbf{v}_i$ sorted from the largest to the smallest. This dyadic coherence can be related to a variance $\sigma^2 = 1 - \beta_1 = \beta_2 + \beta_3$, and thus to the radius of a cone of uncertainty around the eigenvector $\mathbf{v}_i$. Therefore, the dyadic coherence leads to a circular cone of uncertainty whereas the projection of the covariance matrix leads to an ellipsoidal cone of uncertainty, which is a more detailed description of variability.

V. EXPERIMENTAL RESULTS

In this section, we use the presented framework to build and study a statistical atlas of DT-MRIs for a better understanding of the cardiac fiber architecture and of its variability within a population of nine canine hearts. We propose preliminary studies to bridge the gap between statistical models, synthetic models and patient-specific models. First, we construct the statistical atlas of canine hearts. Second, we compare this atlas with a synthetic model of mammalian hearts to evaluate the relevance of the simplifications made when building the synthetic description of the fiber orientation. Finally, we proceed to an inter-species comparison between the canine hearts and a human heart. It provides a preliminary evaluation of the relevance to use canine hearts for clinical applications. This is a first step towards further studies with larger databases.

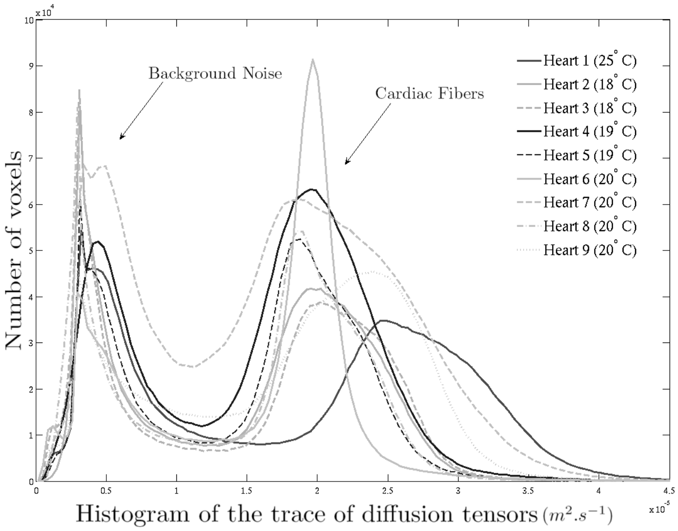

Fig. 8. Histograms of the trace of the diffusion tensors in each heart acquired at different temperatures. The DT-MRIs are normalized to better capture the intrinsic variability between hearts.

A. Data Acquisition

We used a DT-MRI dataset of *ex vivo* fixed normal hearts (9 canine and 1 human hearts) acquired by the Center of Cardiovascular Bioinformatics and Modeling (CCBM) at the Johns Hopkins University [18] and available on the internet[2]. Each heart was placed in an acrylic container filled with Fomblin, a perfluoropolyether (Ausimon, Thorofare, NJ). Fomblin has a low dielectric effect and minimal MR signal thereby increasing contrast and eliminating unwanted susceptibility artifacts near the boundaries of the heart. The long axis of the hearts were aligned with the z-axis of the scanner. Images were acquired with a 4-element knee phased array coil on a 1.5 T GE CV/i MRI Scanner (GE, Medical System, Wausheka, WI) using a gradient system (from 14 to 28 gradients) with 40 mT/m maximum gradient amplitude and a 150 T/m/s slew rate. The resolution of the images are around $0.3 \times 0.3 \times 0.9$ mm^3 per voxel. The temperature during acquisition was different from one heart to another in a range from 18 to $25°$C.

B. Pre-Processing Data

We apply a basic threshold with the Log-Euclidean norm of the diffusion tensors to separate the heart from the background noise. The histogram of the trace of the diffusion tensors shows that there is an important dispersion which is not necessarily due to an intrinsic variability between hearts (see Fig. 8). For instance, the temperature of acquisition can be different. We perform a global normalization of the mean value of the diffusion tensors norm to minimize the influence of this

---

[2] http://www.ccbm.jhu.edu/research/DTMRIDS.php

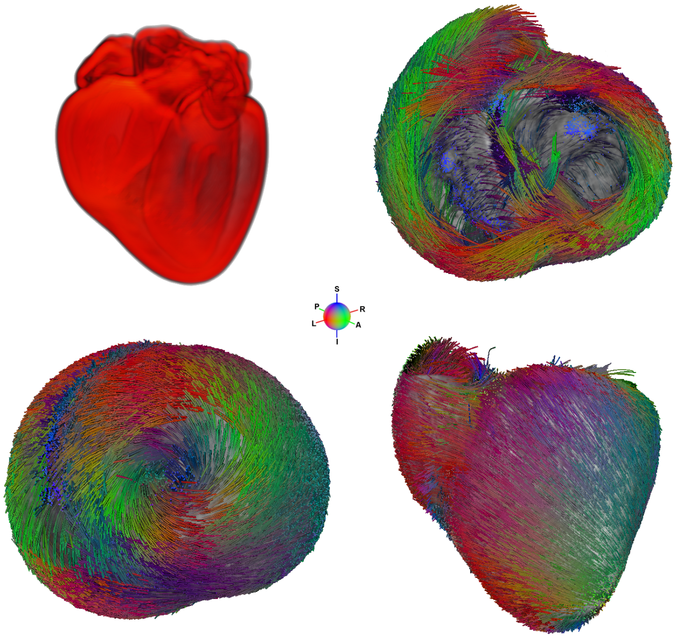

Fig. 9. [*Upper Left*] Average geometry from the anatomical MRIs. [*Others*] Top (*Upper Right*), side (*Lower Right*) and bottom (*Lower Left*) views of fiber tracking computed on the average DT-MRI. The colors describe the orientation of the primary eigenvector according to the color sphere (visualization and tensor processing were performed with MedINRIA available at http://www-sop.inria.fr/asclepios/software/MedINRIA/). Atlas data are available on the internet at http://www-sop.inria.fr/asclepios/data/heart.

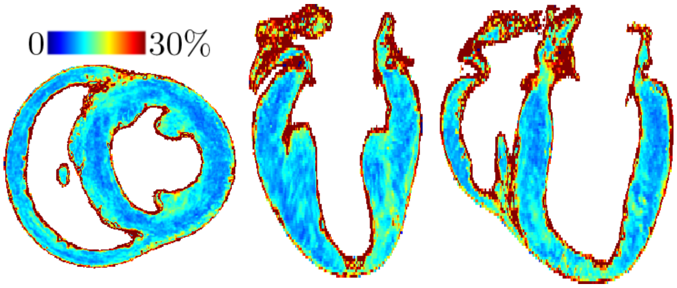

Fig. 10. Global variability $\sqrt{Tr(\Sigma)}$ (homogeneous to a ratio and expressed as a percentage) of the whole tensor in three different orthogonal views: a short axis view and 2 long axis views.

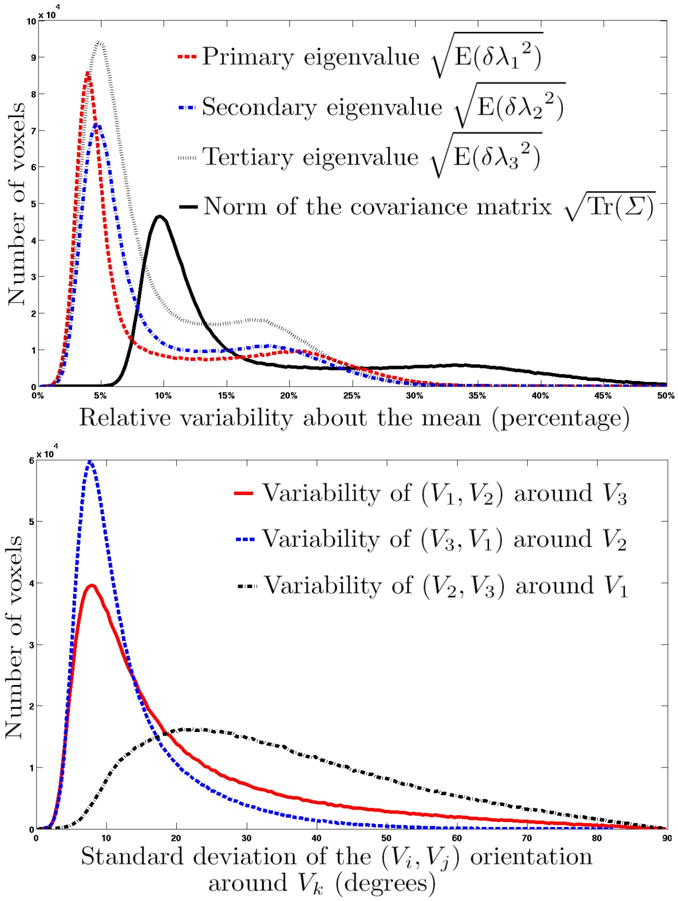

Fig. 11. [*First Row*] Histograms of the global variability $\sqrt{Tr(\Sigma)}$ of the whole diffusion tensor (homogeneous to a ratio and expressed as a percentage) and the variability of the primary, secondary and tertiary eigenvalues in the Log-space $\{\sqrt{E(\delta\lambda_i{}^2)}\}_{i=1,2,3}$ which are also the relative variability of the eigenvalues in the Euclidean space. [*Second Row*] Histograms of the standard deviations of the (V_1, V_2) frame orientation around V_3, the (V_3, V_1) frame orientation around V_2 and the (V_2, V_3) frame orientation around V_1 eigenvectors (angles in degrees).

dispersion. Thus, the inter-subject statistical analysis of the eigenvalues provides an information about the dispersion of the diffusion rates over the space. To include realistic averaged diffusion rates, we scale the eigenvalues of the DT-MRI atlas with the Log-Euclidean mean (which is the geometric mean in a one dimension space) of all these normalization factors.

C. Statistical Atlas

We applied the proposed framework to the dataset of nine canine hearts presented previously. We obtain an average geometry (see Fig. 9) and a smooth cardiac DT-MRI atlas. In Fig. 10, we can observe the norm of the covariance matrix showing a global stability of the compact myocardium and several variable regions, especially at the RV and LV endocardial apices where the fiber structure is probably less organized. Some other variabilities at the surface of the heart are also due to acquisition and registration artifacts. The histogram of the norm of the covariance matrix (see Fig. 11) shows an average variability of the whole diffusion tensor of around 10%.

In order to have a better interpretation of this covariance matrix and to understand the origin of the variabilities, we project it onto the orthonormal basis $\{W_i\}_{i=1,\ldots 6}$ of the tangent space at the mean diffusion tensor. In Fig. 12, we can observe the spatial distribution of the variability of the eigenvalues. The percentages of variability of the 1st, 2nd and 3rd eigenvalues are mostly lower than 10% in the compact myocardium (see Fig. 11). The variabilities of the diffusion rates are homogeneous over the heart and stable within the population.

Extracting the variability of the eigenvectors orientation is important to evaluate the variability of the myocardial fiber architecture. As shown in Figs. 11 and 13, the mode of the standard deviations are 7.9 and 7.7 degrees for the two rotations around the secondary and tertiary eigenvectors in the planes containing the primary eigenvector. These two values describe the dispersion of the fiber orientation that appears to

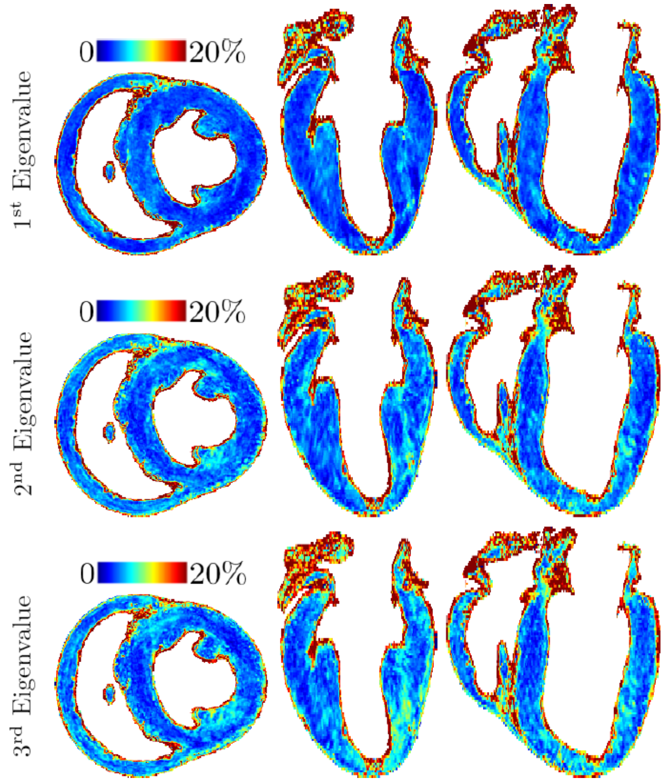

Fig. 12. Relative variabilities of the primary, secondary and tertiary eigenvalues $\{\sqrt{E(\delta\lambda_i{}^2)}\}_{i=1,2,3}$ about their respective mean. These variabilities are shown in three different orthogonal views: a short axis view and 2 long axis views.

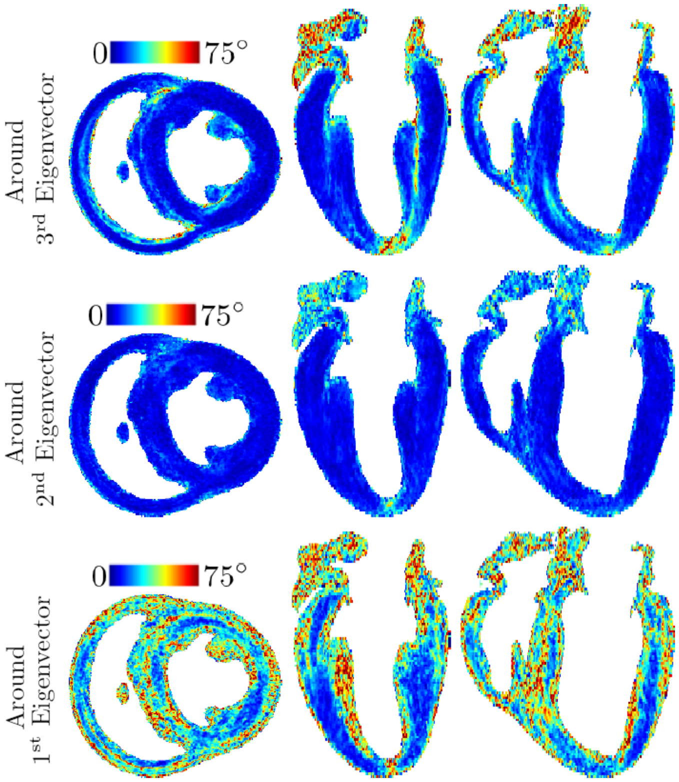

Fig. 13. Standard deviation of the (V_1, V_2) frame orientation around V_3, the (V_3, V_1) frame orientation around V_2 and the (V_2, V_3) frame orientation around V_1 eigenvectors (angles in degrees). These variabilities are shown in three different orthogonal views: a short axis view and 2 long axis views.

be consistent within the population.

The orientation of the laminar sheets described by the rotation of the plane Span$(\mathbf{v}_2, \mathbf{v}_3)$ around $\mathbf{v}_1$ shows a much higher mode of the standard deviation with 22.7 degrees. Mostly located in the sub-epicardium and sub-endocardium of the left ventricle, these high variabilities of the laminar sheet orientations could be due to the presence of two populations of symmetric laminar sheets in the same heart [18]. The existence of these two populations was explained as the optimal configurations of the fibers to maximize the systolic shear [53]. Second, since the secondary and tertiary eigenvalues are closer one to each other than to the primary eigenvalue, we can expect to have a low confidence in their definition. But a low confidence in their definition means either that there is no laminar sheets structure, or that diffusion tensors cannot model the presence of two populations of laminar sheets in the voxel. Beside these high variabilities in the sub-epicardium and sub-endocardium, the laminar sheet orientations are still globally less consistent within the population than the fiber orientation.

D. *Comparison of the Atlas with a Synthetic Model*

Synthetic models of the cardiac fiber architecture, formulated by analytical laws, are usually built from common features observed on mammalian hearts and formulated by analytical laws that simplify the reality. The synthetic model proposed in [8] describes the fiber orientations in an ellipsoidal template geometry of the ventricles. Since this synthetic description is simply a vector field of the fiber orientation, we only use the primary eigenvector of the statistical atlas. We compare the histograms of the angular difference and its Mahalanobis distance between the fiber orientations of the synthetic model and the atlas. In Table I and Figs. 14 and 15, we observe that the distribution modes of the synthetic model (19.6 degrees and 0.95 times the standard deviation) are higher than the distribution modes of the canine hearts (6.9 degrees and 0.58 times the standard deviation). The synthetic model is clearly outside of the population of canine hearts. The ellipsoidal geometry and the fiber orientations of the synthetic model are not accurate enough to catch all their subtle variations. For instance, in the short axis view the discontinuity at the crossing of the two ventricular walls is not realistic [54]. Moreover, the synthetic description reaches its limits at the right ventricular and left ventricular apices where the modeling probably needs different analytical laws from the compact myocardium.

E. *Comparison of the Atlas with a Human Heart*

There is no *in vivo* access to high resolution data and normal hearts are preferred to be transplanted rather than used for research purposes. Since studies of cardiac fiber architecture are mainly based on dissections and *ex vivo* DT-MRI acquisitions of other mammalians, comparing the statistical canine atlas with a human data gives the opportunity

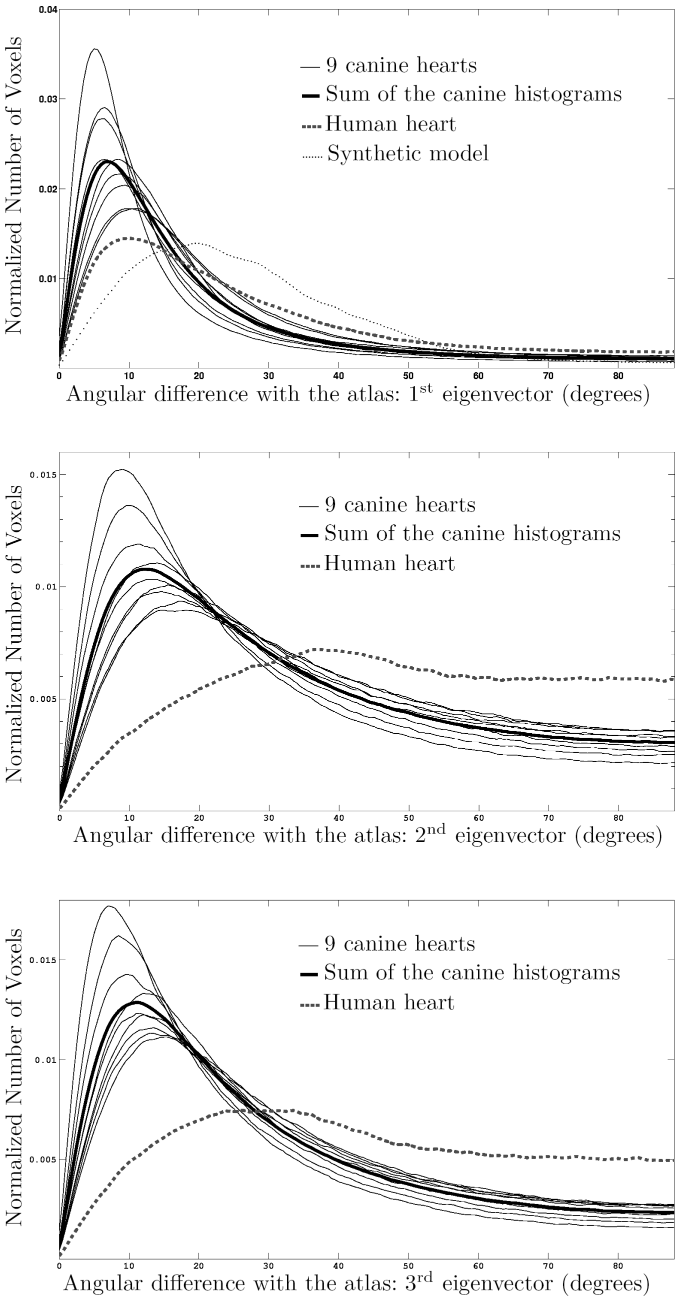

Fig. 14. Normalized histograms of the angular difference (degrees) of the primary, secondary and tertiary eigenvectors between the atlas and: the canine hearts, the human heart and the synthetic model.

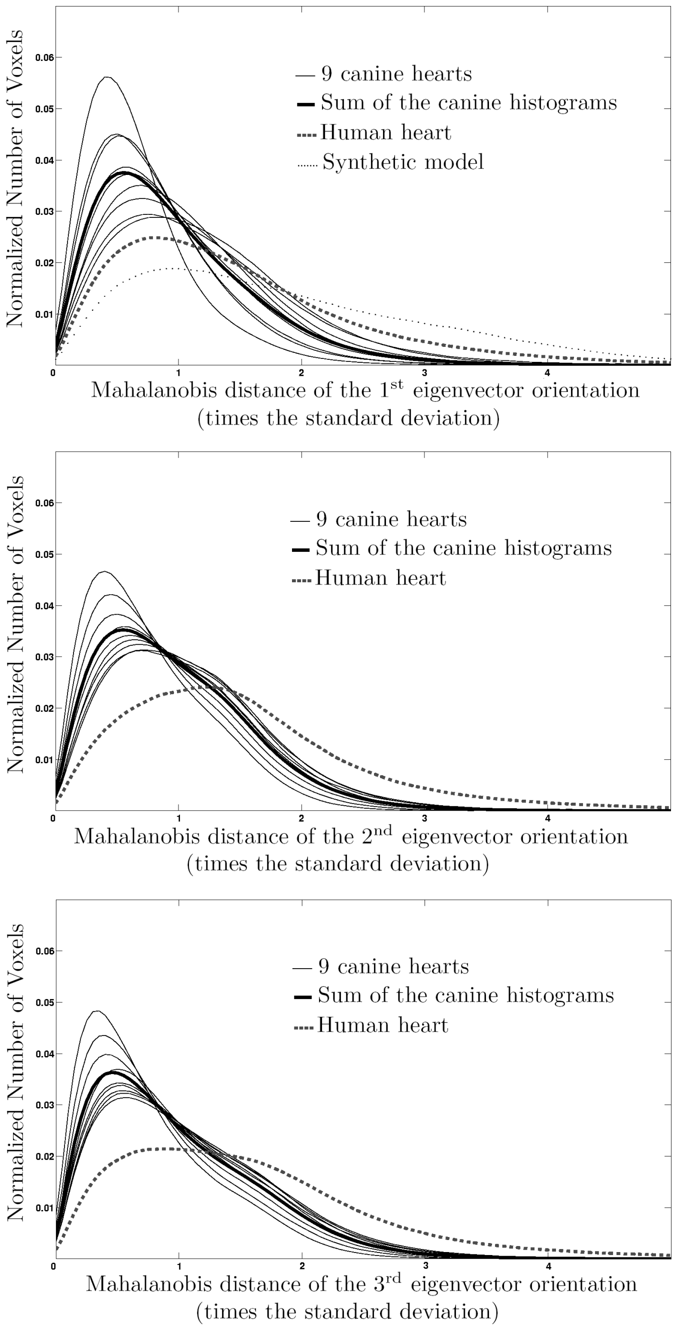

Fig. 15. Mahalanobis distance of the angular difference (times the standard deviation) of the primary, secondary and tertiary eigenvectors between the atlas and: the canine hearts, the human heart and the synthetic model.

to provide preliminary results on the relevance of using prior knowledge from canine data in clinical applications.

Only one human heart is available in the JHU database, and even if it is a high quality acquisition, the quality of the heart itself is not as good as the canine ones due to its previous usage for clinical applications. It limits the conclusion of this study but since it is rare to have access to human data at high resolution, it is a first step towards a more exhaustive inter-species comparison of the cardiac fiber architecture.

We register the human data on the statistical atlas according to the steps described in the Sections II and III to be consistent with the atlas building framework. Then, we perform a statistical comparison at each voxel. First, we compute the normalized Mahalanobis distance μ [29]:

$$\breve{\mu}^2_{(\overline{D}_{\log}, D_{\text{human}})} = \frac{1}{M}\text{vec}(\Delta D)^t \cdot \Sigma^{-1} \cdot \text{vec}(\Delta D)$$

where $\Delta D = \log(D_{\text{human}}) - \log(\overline{D}_{\log})$ and $M = 6$ the dimension of the diffusion tensor space.

The mode of the normalized Mahalanobis distance is 1.49 whereas it is lower than 1 for canine hearts of the dataset. To have a better understanding of the origin of this differ-

Eigenvector/Heart	Canine Hearts	Human Heart	Synthetic Model
Primary	6.9° - 0.58	10.1° - 0.81	19.6° - 0.95
Secondary	11.6° - 0.57	36.2° - 1.15	-
Tertiary	11.4° - 0.46	29.1° - 1.09	-

TABLE I
DISTRIBUTION MODES OF THE ANGULAR DIFFERENCES BETWEEN THE EIGENVECTORS (DEGREES) AND OF THEIR CORRESPONDING MAHALANOBIS DISTANCES (TIMES THE STANDARD DEVIATION).

ence, we compare the eigenvalues and the orientation of the eigenvectors (see Figs. 14 and 15). The mode of the angular differences of the primary, secondary and tertiary eigenvectors are respectively 10.1, 36.2 and 29.1 degrees. To compare these differences with the variability of the canine population, we compute the Mahalanobis distance of these orientation parameters that are respectively 0.81, 1.15 and 1.09 times the standard deviation (see Table I). These results confirm that the fiber orientations between human and canine hearts are more consistent than the laminar sheet orientations.

VI. CONCLUSION AND PERSPECTIVES

We presented a computational framework to build a statistical atlas of cardiac fiber architecture based on DT-MRIs. We used most recent advances in diffusion tensor statistics to propose new complete and consistent tools to translate their covariance matrix into the variances of the eigenvectors and eigenvalues. These tools are well-suited to study the variability of cardiac fibers and laminar sheets within a population.

The registration strategy we proposed for atlas building is not the only one fitting to our framework. Studying the choice of the registration algorithm on the diffusion tensor statistics could help in refining the quality of the results. Furthermore, most recent advances in statistics on diffeomorphisms [51] will improve the consistency of the registration framework. One could also think about improving initialization step by adding a polyaffine registration [55] to better match the main cardiac structures as the ventricles and the atria.

We emphasized the differences of two common different reorientation strategies when transforming the diffusion tensors. The *Finite Strain* (FS) reorientation strategy is a geometric transformation preserving the gradient of diffusion tensors. It seems more suited to the comparison of geometric parameters of diffusion tensor fields. On the other hand, the *Preservation of the Principal Direction* (PPD) is a mechanical transformation of the underlying structure. This strategy is preferred for the comparison of diffusion tensor fields when their registration really has an underlying mechanical meaning.

We believe that this statistical atlas[3] will lead to a better understanding of the cardiac fiber architecture. For instance, the application of this framework to nine canine hearts confirms the already established stronger intra-species stability of fiber orientations than laminar sheet orientations. As preliminary results of an inter-species comparison between a human heart and the statistical atlas of canine hearts, we observe the good inter-species stability of the fiber orientations. Of course, the access to a larger database will provide more reliable inter- and intra-species statistics. A better understanding of the inter-species differences would help for instance to extend experimental results from one species to another. Building and comparing statistical atlases of normal and pathological hearts could also help in a better quantification of the pathology, for instance in the remodeling process.

Moreover, such a statistical atlas offers a valuable prior knowledge in the context of electromechanical modeling of the heart. The information about the laminar sheets is particularly relevant since it has been shown to influence significantly the cardiac motion [53], [56], in particular the wall thickening and the apico-basal torsion [3]. A precise study of the impact of the cardiac fiber architecture on the electromechanical simulations would make it possible to design the best fiber model for simulation-based clinical applications.

APPENDIX A
PROJECTIONS OF THE COVARIANCE MATRIX

Let us consider the dyadic tensor decomposition of the average diffusion tensor in the Log-space:

$$\overline{W} = \log(\overline{D}_{\log}) = \sum_{i=1}^{3} \lambda_i \mathbf{v}_i \cdot \mathbf{v}_i{}^t$$

where $\lambda_i = \log(d_i)$ and the $\{d_i\}_{i=1,2,3}$ are the eigenvalues of the diffusion tensor $\overline{D}_{\log}$. Considering the deviations $\delta\lambda_i$ and $\delta\mathbf{v}_i$ of the eigenvalues λ_i and the eigenvectors $\mathbf{v}_i$ around the mean diffusion tensor, the previous expresion becomes:

$$\overline{W} + \delta W = \sum_{i=1}^{3} (\lambda_i + \delta\lambda_i)(\mathbf{v}_i + \delta\mathbf{v}_i).(\mathbf{v}_i + \delta\mathbf{v}_i)^t$$

Let us consider the increment ε_{ij} of each vector $\delta\mathbf{v}_i$ in the frame of the mean eigenvectors $\{\mathbf{v}_j\}_{j=1,2,3}$:

$$\begin{aligned} \delta\mathbf{v}_1 &= \varepsilon_{11}\mathbf{v}_1 + \varepsilon_{12}\mathbf{v}_2 + \varepsilon_{13}\mathbf{v}_3 \\ \delta\mathbf{v}_2 &= \varepsilon_{21}\mathbf{v}_1 + \varepsilon_{22}\mathbf{v}_2 + \varepsilon_{23}\mathbf{v}_3 \\ \delta\mathbf{v}_3 &= \varepsilon_{31}\mathbf{v}_1 + \varepsilon_{32}\mathbf{v}_2 + \varepsilon_{33}\mathbf{v}_3 \end{aligned}$$

These coordinates ε_{ij} in the frame of the mean eigenvectors $\{\mathbf{v}_j\}_{j=1,2,3}$ correspond to the tangent of the angle between $\mathbf{v}_i + \delta\mathbf{v}_i$ and $\mathbf{v}_j$. Since $\mathbf{v}_1$,$\mathbf{v}_2$ and $\mathbf{v}_3$ form an orthonormal frame of $\mathbb{R}^3$, $\varepsilon_{ij} = -\varepsilon_{ji}$ at the first order:

$$\begin{gathered} (\mathbf{v}_i + \delta\mathbf{v}_i)^t \cdot (\mathbf{v}_j + \delta\mathbf{v}_j) = (1+\varepsilon_{ii})\varepsilon_{ji} + (1+\varepsilon_{jj})\varepsilon_{ij} = 0 \\ (1+\varepsilon_{ii})\varepsilon_{ji} + (1+\varepsilon_{jj})\varepsilon_{ij} + o(\varepsilon_{ij}, \varepsilon_{ji}) = 0 \\ \varepsilon_{ij} + \varepsilon_{ji} = o(\varepsilon_{ij}, \varepsilon_{ji}) \end{gathered}$$

Furthermore, the $\{\mathbf{v}_i + \delta\mathbf{v}_i\}_{i=1,2,3}$ are unit vectors. It means there is a relationship between ε_{i1}, ε_{i2} and ε_{i3}:

$$(1+\varepsilon_{i1})^2 + \varepsilon_{i2}^2 + \varepsilon_{i3}^2 = 1$$

Thus, $\varepsilon_{ii} = -\frac{1}{2}(\varepsilon_{im}^2 + \varepsilon_{in}^2) + o(\varepsilon_{im}^2, \varepsilon_{in}^2)$ which means that we can consider that $\varepsilon_{ii} = 0$ at the first order.

Finally, considering the first order terms we obtain the following expression:

$$\begin{aligned} \delta W &= \delta\lambda_1 W_1 + \delta\lambda_2 W_2 + \delta\lambda_3 W_3 + \varepsilon_{23}\sqrt{2}(\lambda_2 - \lambda_3)W_4 \\ &+ \varepsilon_{13}\sqrt{2}(\lambda_1 - \lambda_3)W_5 + \varepsilon_{12}\sqrt{2}(\lambda_1 - \lambda_2)W_6 \end{aligned}$$

where the $\{W_i\}_{i=1,2,3}$ form an orthonormal basis of the tangent space at the mean diffusion tensor:

---

[3] available at http://www-sop.inria.fr/asclepios/data/heart

$$\begin{aligned} W_1 &= \mathbf{v}_1 \cdot \mathbf{v}_1{}^t & W_4 &= \frac{1}{\sqrt{2}}(\mathbf{v}_3 \cdot \mathbf{v}_2{}^t + \mathbf{v}_2 \cdot \mathbf{v}_3{}^t) \\ W_2 &= \mathbf{v}_2 \cdot \mathbf{v}_2{}^t & W_5 &= \frac{1}{\sqrt{2}}(\mathbf{v}_3 \cdot \mathbf{v}_1{}^t + \mathbf{v}_1 \cdot \mathbf{v}_3{}^t) \\ W_3 &= \mathbf{v}_3 \cdot \mathbf{v}_3{}^t & W_6 &= \frac{1}{\sqrt{2}}(\mathbf{v}_2 \cdot \mathbf{v}_1{}^t + \mathbf{v}_1 \cdot \mathbf{v}_2{}^t) \end{aligned}$$

Thus, we can formulate the variances of ε_{12}, ε_{13}, ε_{23}, $\delta\lambda_1$, $\delta\lambda_2$ and $\delta\lambda_3$ with respect to the projections of the covariance matrix onto the orthonormal basis $\{W_i\}_{i=1,\dots 6}$ of the tangent space:

$$\begin{aligned} E(\delta{\lambda_1}^2) &= \text{vec}(W_1)^t \cdot \Sigma \cdot \text{vec}(W_1) \\ E(\delta{\lambda_2}^2) &= \text{vec}(W_2)^t \cdot \Sigma \cdot \text{vec}(W_2) \\ E(\delta{\lambda_3}^2) &= \text{vec}(W_3)^t \cdot \Sigma \cdot \text{vec}(W_3) \end{aligned}$$

$$\begin{aligned} E(\varepsilon_{23}^2) &= \frac{1}{2(\lambda_2 - \lambda_3)^2}[\text{vec}(W_4)^t \cdot \Sigma \cdot \text{vec}(W_4)] \\ E(\varepsilon_{13}^2) &= \frac{1}{2(\lambda_1 - \lambda_3)^2}[\text{vec}(W_5)^t \cdot \Sigma \cdot \text{vec}(W_5)] \\ E(\varepsilon_{12}^2) &= \frac{1}{2(\lambda_1 - \lambda_2)^2}[\text{vec}(W_6)^t \cdot \Sigma \cdot \text{vec}(W_6)] \end{aligned}$$

APPENDIX B
AFFINE TRANSFORMATION OF A PLANE

The affine transformation of the parameters of a plane is known since a long time. We present here a simple demonstration provided in [57].

Let P be a plane and its normal $\mathbf{n}$. The affine transformations preserve the parallelism and therefore the image of a plane is plane. It means that every vector $\mathbf{v}$ in the plane P is transformed through an affine transformation A into a vector $\mathbf{v}' = A\mathbf{v}$ in the image plane P' (see Fig. 16). By definition, every vector $\mathbf{v}$ in the plane P is orthogonal to its normal: $\mathbf{v}^t \cdot \mathbf{n} = 0$. We can write $\mathbf{v}^t \cdot \mathbf{n} = 0$ as follows: $\mathbf{n}^t(A^{-1}A)\mathbf{v} = 0$. A modification of this expression leads to $((A^{-1})^t\mathbf{n})^t \cdot A\mathbf{v} = 0$ and thus to $((A^{-1})^t\mathbf{n})^t \cdot \mathbf{v}' = 0$ which is the definition of a vector orthogonal to the plane P'. Finally, the normal $\mathbf{n}'$ of the image plane P' is given by $\mathbf{n}' = \dfrac{(A^{-1})^t\mathbf{n}}{\|(A^{-1})^t\mathbf{n}\|}$.

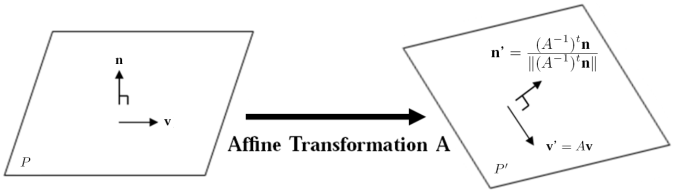

Fig. 16. Affine transformation of a plane P with normal $\mathbf{n}$ into a plane P' with normal $\mathbf{n}'$.

ACKNOWLEDGMENT

This research work was funded by Siemens Corporate Research, Princeton, NJ, USA. Acquisition of the DT-MRIs data was funded by the Intramural Research Program of the National Heart Lung and Blood Institute (E. R. McVeigh Z01-HL4004609). We thank Drs. Patrick A. Helm and Raimond L. Winslow at the Center for Cardiovascular Bioinformatics and Modeling for provision of data, P. Fillard and N.Toussaint for provision of diffusion tensors and fiber tracking computation and visualization tools (available at http://www-sop.inria.fr/asclepios/software/MedINRIA/), and I. J. LeGrice for provision of an illustration in Fig. 4.

REFERENCES

[1] I. J. LeGrice, B. H. Smaill, L. Z. Chai, S. G. Edgar, J. B. Gavin, and P. J. Hunter, “Laminar Structure of the Heart: Ventricular Myocyte Arrangement and Connective Tissue Architecture in the Dog.” *American Journal of Physiology - Heart and Circulatory Physiology*, vol. 269, no. 2, pp. H571–H582, 1995.

[2] K. D. Costa, Y. Takayama, A. D. McCulloch, and J. W. Covell, “Laminar Fiber Architecture and Three-Dimensional Systolic Mechanics in Canine Ventricular Myocardium.” *American Journal of Physiology - Heart and Circulatory Physiology*, vol. 276, pp. H595–H607, 1999.

[3] K. D. Costa, J. W. Holmes, and A. D. McCulloch, “Modelling Cardiac Mechanical Properties in Three Dimensions.” *Philosophical Transactions of the Royal Society A: Mathematical, Physical and Engineering Sciences*, vol. 359, pp. 1233–1250, 2001.

[4] N. Ayache, *Computational Models for the Human Body.*, ser. Handbook of Numerical Analysis, P. Ciarlet, Ed. Amsterdam, The Netherlands: Elsevier, 2004.

[5] F. Sachse, Ed., *Computational Cardiology - Modeling of Anatomy, Electrophysiology, and Mechanics.*, ser. Lecture Notes in Computer Science. New-York: Springer-Verlag Berlin Heidelberg, 2004, vol. 2966.

[6] W.-Y. I. Tseng, T. G. Reese, R. M. Weisskoff, and V. J. Wedeen, “Cardiac Diffusion Tensor MRI In Vivo without Strain Correction.” *Magnetic Resonance in Medicine*, vol. 42, no. 2, pp. 393–403, 1999.

[7] J. Dou, T. G. Reese, W.-Y. I. Tseng, and V. J. Wedeen, “Cardiac Diffusion MRI without Motion Effects.” *Magnetic Resonance in Medicine*, vol. 48, no. 1, pp. 105–114, 2002.

[8] M. Sermesant, K. Rhode, G. I. Sanchez-Ortiz, O. Camara, R. Andriantsimiavona, S. Hegde, D. Rueckert, P. Lambiase, C. Bucknall, E. Rosenthal, H. Delingette, D. L. Hill, N. Ayache, and R. Razavi, “Simulation of Cardiac Pathologies Using an Electromechanical Biventricular Model and XMR Interventional Imaging.” *Medical Image Analysis*, vol. 5, no. 9, pp. 467–80, 2005.

[9] M. Sermesant, P. Moireau, O. Camara, J. Sainte-Marie, R. Andriantsimiavona, R. Cimrman, D. L. Hill, D. Chapelle, and R. Razavi, “Cardiac Function Estimation from MRI Using a Heart Model and Data Assimilation: Advances and Difficulties.” *Medical Image Analysis*, vol. 10, no. 4, pp. 642–656, 2006.

[10] D. Streeter, *Handbook of Physiology*. Williams & Wilkins, 1979, ch. The Cardiovascular System: Gross Morphology and Fiber Geometry of the Heart.

[11] P. Nielsen, I. L. Grice, B. Smail, and P. Hunter, “Mathematical Model of Geometry and Fibrous Structure of the Heart.” *American Journal of Physiology - Heart and Circulatory Physiology*, vol. 260, no. 29, pp. H1365–H1378, 1991.

[12] A. Pitiot, E. Bardinet, P. M. Thompson, and G. Malandain, “Piecewise Affine Registration of Biological Images for Volume Reconstruction,” *Medical Image Analysis*, vol. 10, no. 3, pp. 465–483, 2006.

[13] P. Basser, J. Mattiello, and D. LeBihan, “MR Diffusion Tensor Spectroscopy and Imaging.” *Biophysical Journal*, vol. 66, pp. 259–267, 1994.

[14] E. W. Hsu and C. S. Henriquez, “Myocardial Fiber Orientation Mapping Using Reduced Encoding Diffusion Tensor Imaging.” *Journal of Cardiovascular Magnetic Resonance*, vol. 3, no. 4, pp. 339–2347, 2001.

[15] D. F. Scollan, A. Holmes, R. L. Winslow, and J. Forder, “Histological Validation of Myocardial Microstructure Obtained from Diffusion Tensor Magnetic Resonance Imaging.” *American Journal of Physiology - Heart and Circulatory Physiology*, vol. 275, pp. H2308–H2318, 1998.

[16] E. W. Hsu, A. L. Muzikant, S. A. Matulevicius, R. C. Penland, and C. S. Henriquez, “Magnetic Resonance Myocardial Fiber-Orientation Mapping with Direct Histological Correlation.” *American Journal of Physiology - Heart and Circulatory Physiology*, vol. 274, pp. H1627–H1634, 1998.

[17] W. Y. Tseng, V. J. Wedeen, T. G. Reese, R. N. Smith, and E. F. Halpern, “Diffusion Tensor MRI of Myocardial Fibers and Sheets: Correspondence with Visible Cut-Face Texture.” *Journal of Magnetic Resonance Imaging*, vol. 17, no. 1, pp. 31–42, 2003.

[18] P. A. Helm, H. J. Tseng, L. .Younes, E. R. McVeigh, and R. L. Winslow, “Ex Vivo 3D Diffusion Tensor Imaging and Quantification of Cardiac Laminar Structure.” *Magnetic Resonance in Medicine*, vol. 54, no. 4, pp. 850–859, 2005.

[19] P. A. Helm, M. F. Beg, M. I. Miller, and R. L. Winslow, “Measuring and Mapping Cardiac Fiber and Laminar Architecture Using Diffusion Tensor MR Imaging.” *Annals of the New-York Academy of Science*, vol. 1047, pp. 296–307, 2005.

[20] L. Geerts, P. Bovendeerd, K. Nicolay, and T. Arts, “Characterization of the Normal Cardiac Myofiber Field in Goat Measured with MR-Diffusion Tensor Imaging.” *American Journal of Physiology - Heart and Circulatory Physiology*, vol. 283, no. 1, pp. H139–H145, 2002.

[21] P. Helm, “A Novel Technique for Quantifying Variability of Cardiac Anatomy: Application to the Dyssynchronous Failing Heart.” Ph.D. dissertation, Johns Hopkins University, 2005.

[22] H. Sundar, D. Shen, G. Biros, H. Litt, and C. Davatzikos, “Estimating Myocardial Fiber Orientation by Template Warping.” in *3rd IEEE International Symposium on Biomedical Imaging (ISBI’06)*, 2006, pp. 73–76.

[23] S. H. Gilbert, A. P. Benson, P. Li, and A. V. Holden, “Visualisation of Dog Myocardial Structure from Diffusion Tensor Magnetic Resonance Imaging: The Paradox of Uniformity and Variability.” in *Proceedings of the 4th International Conference on Functional Imaging and Modeling of the Heart (FIMH’07)*, vol. 4466 of LNCS, 2007, pp. 403–412.

[24] I. Legrice, P. Hunter, and B. Smaill, “Laminar Structure of the Heart: a Mathematical Model.” *American Journal of Physiology - Heart and Circulatory Physiology*, vol. 272, no. 5 Part 2, pp. H2466–H2476, 1997.

[25] A. McCulloch, J. Bassingthwaighte, P. Hunter, D. Noble, T. Blundell, and T. Pawson, “Computational biology of the heart: From structure to function.” *Progress in Biophysics & Molecular Biology*, vol. 69, no. 2/3, 1998.

[26] R. Burtin, G. Plank, J. Schneider, V. Grau, H. Ahammer, S. Keeling, J. Lee, N. Smith, D. Gavaghan, N. Trayanova, and P. Kohl, “Three-Dimensional Models of Individual Cardiac Histoanatomy: Tools and Challenges.” *Annals of the New-York Academy of Science*, vol. 1080, pp. 301–319, 2006.

[27] M. Moakher, “A Differential Geometric Approach to the Geometric Mean of Symmetric Positive-Definite Matrices.” *SIAM - Journal on Matrix Analysis and Applications*, vol. 26, no. 3, pp. 735–747, 2005.

[28] P. G. Batchelor, M. Moakher, D. Atkinson, F. Calamante, and A. Connelly, “A Rigorous Framework for Diffusion Tensor Calculus.” *Magnetic Resonance in Medicine*, vol. 53, pp. 221–225, 2005.

[29] X. Pennec, P. Fillard, and N. Ayache, “A Riemannian Framework for Tensor Computing.” *International Journal of Computer Vision*, vol. 66, no. 1, pp. 41–66, 2006.

[30] C. Lenglet, M. Rousson, R. Deriche, and O. Faugeras, “Statistics on the Manifold of Multivariate Normal Distributions: Theory and Application to Diffusion Tensor MRI Processing.” *Journal of Mathematical Imaging and Vision*, vol. 25, no. 3, pp. 423–444, 2006.

[31] P. T. Fletcher and S. C. Joshi, “Riemannian geometry for the statistical analysis of diffusion tensor data.” *Signal Processing*, vol. 87, no. 2, pp. 250–262, 2007.

[32] V. Arsigny, P. Fillard, X. Pennec, and N. Ayache, “Log-Euclidean Metrics for Fast and Simple Calculus on Diffusion Tensors.” *Magnetic Resonance in Medicine*, vol. 56, no. 2, pp. 411–421, 2006.

[33] D. K. Jones, L. D. Griffin, D. C. Alexander, M. Catanie, M. A. Horsfield, R. Howarda, and S. C. R. Williams, “Spatial Normalization and Averaging of Diffusion Tensor MRI Data Sets.” *NeuroImage*, vol. 17, pp. 592–617, 2002.

[34] P. J. Basser and S. Pajevic, “Statistical Artifacts in Diffusion Tensor MRI (DT-MRI) caused by Background Noise.” *Magnetic Resonance in Medicine*, vol. 44, no. 1, pp. 41–50, 2000.

[35] Y. Masutani, S. Aoki, O. Abe, and K. Ohtomo, “Model-Based Tractography Based on Statistical Atlas of MR-DTI.” in *3rd IEEE International Symposium on Biomedical Imaging (ISBI’06)*, 2006, pp. 89–92.

[36] C. Goodlett, B. Davis, R. Jean, J. Gilmore, and G. Gerig, “Improved Correspondence for DTI Population Studies via Unbiased Atlas Building.” in *Proceedings of the 9th International Conference on Medical Image Computing and Computer-Assisted Intervention (MICCAI’06)*, vol. 4191 of LNCS, 2006, pp. 260–267.

[37] J.-M. Peyrat, M. Sermesant, X. Pennec, H. Delingette, C. Xu, E. R. McVeigh, and N. Ayache, “Towards a Statistical Atlas of Cardiac Fiber Structure.” in *Proceedings of the 9th International Conference on Medical Image Computing and Computer-Assisted Intervention (MICCAI’06)*, vol. 4190 of LNCS, 2006, pp. 297–304.

[38] A. Azar, C. Xu, X. Pennec, and N. Ayache, “An Interactive Intensity- and Feature-Based Non-Rigid Registration Framework for 3D Medical Images.” in *3rd IEEE International Symposium on Biomedical Imaging (ISBI’06)*, 2006, pp. 824–827.

[39] A. Guimond, J. Meunier, and J.-P. Thirion, “Average Brain Models: A Convergence Study.” *Computer Vision and Image Understanding*, vol. 77, no. 2, pp. 192–210, 2000.

[40] D. C. Alexander, C. Pierpaoli, P. J. Basser, and J. C. Gee, “Spatial Transformations of Diffusion Tensor Magnetic Resonance Images.” *IEEE Transactions on Medical Imaging*, vol. 20, no. 11, pp. 1131–1139, 2001.

[41] A. Guimond, C. R. G. Guttmann, S. K. Warfield, and C.-F. Westin, “Deformable Registration of DT-MRI Data Based on Transformation Invariant Tensor Characteristics.” in *1st IEEE International Symposium on Biomedical Imaging (ISBI’02)*, 2002, pp. 761–764.

[42] J. Ruiz-Alzola, C.-F. Westin, S. K. Warfield, C. Alberola, S. E. Maier, and R. Kikinis, “Nonrigid Registration of 3D Tensor Medical Data.” *Medical Image Analysis*, vol. 6, no. 2, pp. 143–161, 2002.

[43] H. Zhang, P. A. Yushkevich, D. C. Alexander, and J. C. Gee., “Deformable Registration of Diffusion Tensor MR Images with Explicit Orientation Optimization.” *Medical Image Analysis*, vol. 10, no. 5, pp. 765–785, 2002.

[44] Y. Cao, M. I. Miller, S. Mori, R. L. Winslow, and L. Younes, “Diffeomorphic Matching of Diffusion Tensor Images.” in *Proceedings of the 2006 Conference on Computer Vision and Pattern Recognition Workshop (CVPRW06)*, 2006, pp. 67–67.

[45] M. F. Beg, P. A. Helm, E. R. McVeigh, M. I. Miller, and R. L. Winslow, “Computational Cardiac Anatomy Using MRI.” *Magnetic Resonance in Medicine*, vol. 52, no. 5, pp. 1167–1174, 2004.

[46] F. Bookstein, “Principal Warps: Thin-Plate Splines and the Decomposition of Deformations,” *IEEE Transactions on Pattern Analysis and Machine Intelligence*, vol. 11, no. 6, pp. 567–585, 1989.

[47] C. Chefd’hotel, G. Hermosillo, and O. Faugeras, “Flows of Diffeomorphisms for Multimodal Image Registration.” in *1st IEEE International Symposium on Biomedical Imaging (ISBI’02)*, 2002, pp. 753–756.

[48] P. A. Helm, L. Younes, M. F. Beg, D. B. Ennis, C. Leclercq, O. P. Faris, E. R. McVeigh, D. Kass, and M. I. Miller, “Evidence of Structural Remodeling in the Dyssynchronous Failing Heart.” *Circulation Research*, vol. 98, no. 1, pp. 125–132, 2005.

[49] B. Avants and J. C. Gee, “Shape Averaging with Diffeomorphic Flows for Atlas Creation.” in *2nd IEEE International Symposium on Biomedical Imaging (ISBI’04)*, vol. 1, 2004, pp. 595–598.

[50] S. Joshi, B. Davis, M. Jomier, and G. Gerig, “Unbiased Diffeomorphic Atlas Construction for Computational Anatomy.” *NeuroImage*, vol. 23, no. 1, pp. S151–S160, 2004.

[51] V. Arsigny, O. Commowick, X. Pennec, and N. Ayache, “A Log-Euclidean Framework for Statistics on Diffeomorphisms.” in *Proceedings of the 9th International Conference on Medical Image Computing and Computer-Assisted Intervention (MICCAI’06)*, vol. 4190 of LNCS, 2006, pp. 924–931.

[52] L. Malvern, Ed., *Introduction to the Mechanics of a Continuous Medium*. Englewood Cliffs, NJ: Prentice-Hall, 1969.

[53] T. Arts, K. Costa, J. Covell, and A. McCulloch, “Relating Myocardial Laminar Architecture to Shear Strain and Muscle Fiber Orientation.” *American Journal of Physiology - Heart and Circulatory Physiology*, vol. 280, pp. H2222–H2229, 2001.

[54] J.-M. Peyrat, M. Sermesant, X. Pennec, H. Delingette, C. Xu, E. R. McVeigh, and N. Ayache, “Statistical Comparison of Cardiac Fiber Architectures.” in *Proceedings of the 4th International Conference on Functional Imaging and Modeling of the Heart (FIMH’07)*, vol. 4466 of LNCS, 2007, pp. 413–423.

[55] V. Arsigny, X. Pennec, and N. Ayache, “Polyrigid and Polyaffine Transformations: a Novel Geometrical Tool to Deal with Non-Rigid Deformations - Application to the Registration of Histological Slices.” *Medical Image Analysis*, vol. 9, no. 6, pp. 507–523, 2005.

[56] T. P. Usyk, R. Mazhari, and A. D. McCulloch, “Effect of Laminar Orthotropic Myofiber Architecture on Regional Stress and Strain in the Canine Left Ventricle.” *Journal of Elasticity*, vol. 61, pp. 143–164, 2000.

[57] K. Turkowski, *Graphics Gems*. Academic Press, Inc., 1990, ch. Properties of Surface-Normal Transformations., pp. 539–547.